AASLD
The Liver Meeting®

4th – 8th November
Washington DC

Late Breaking Poster Presentation at The Liver Meeting® 2022

Change in Fibrosis-4 Index over time is associated with subsequent risk of liver events, cardiovascular events, and all-cause mortality in patients with obesity and/or type 2 diabetes

Prof. Quentin M. Anstee

Professor of Experimental Hepatology & Consultant Hepatologist, Faculty of Medical Sciences, Newcastle University, UK

READ MORE

novo nordisk®

ORIGINAL ARTICLE

Myeloid p38 activation maintains macrophage–liver crosstalk and BAT thermogenesis through IL-12–FGF21 axis

María Crespo[1] | Ivana Nikolic[1] | Alfonso Mora[1] | Elena Rodríguez[1] | Luis Leiva-Vega[1] | Aránzazu Pintor-Chocano[1] | Daniel Horrillo[2,3] | Lourdes Hernández-Cosido[4,5] | Jorge L. Torres[6,7] | Eva Novoa[8,9] | Rubén Nogueiras[8,9] | Gema Medina-Gómez[2,3] | Miguel Marcos[6,7] | Magdalena Leiva[1] | Guadalupe Sabio[1]

[1]Centro Nacional de Investigaciones Cardiovasculares, Madrid, Spain

[2]Departamento de Ciencias Básicas de la Salud, Área de Bioquímica y Biología Molecular, Lipobeta group, Universidad Rey Juan Carlos, Madrid, Spain

[3]Laboratorio LAFEMEX, Área de Bioquímica y Biología Molecular, Departamento de Ciencias Básicas de la Salud, Facultad de Ciencias de la Salud, Universidad Rey Juan Carlos, Madrid, Spain

[4]Department of General Surgery, University Hospital of Salamanca-IBSAL, Salamanca, Spain

[5]Department of Surgery, University of Salamanca, Salamanca, Spain

[6]Department of Internal Medicine, University Hospital of Salamanca-Institute of Biomedical Research of Salamanca (IBSAL), Salamanca, Spain

[7]Department of Medicine, University of Salamanca, Salamanca, Spain

[8]Center for Research in Molecular Medicine and Chronic Diseases (CIMUS), University of Santiago de Compostela-Instituto de Investigación Sanitaria, Santiago de Compostela, Spain

[9]CIBER Fisiopatologia de la Obesidad y Nutrición (CIBERobn), Madrid, Spain

Correspondence
Magdalena Leiva and Guadalupe Sabio, Centro Nacional de Investigaciones Cardiovasculares, C/Melchor Fernández Almagro, 3, Madrid 28029, Spain.
Email: magdalena.leiva@cnic.es and guadalupe.sabio@cnic.es

Abstract

Obesity features excessive fat accumulation in several body tissues and induces a state of chronic low-grade inflammation that contributes to the development of diabetes, steatosis, and insulin resistance. Recent research has shown that this chronic inflammation is crucially dependent on p38 pathway activity in macrophages, suggesting p38 inhibition as a possible treatment for obesity comorbidities. Nevertheless, we report here that lack of p38 activation in myeloid cells worsens high-fat diet–induced obesity, diabetes, and steatosis. Deficient p38 activation increases macrophage IL-12 production, leading to inhibition of hepatic FGF21 and reduction of thermogenesis in the brown fat. The implication of FGF21 in the phenotype was confirmed by its specific deletion in hepatocytes. We also found that IL-12 correlates with liver damage in human biopsies, indicating the translational potential of our

Abbreviations: ALT, alanine aminotransferase; Alb-Cre, B6.Cg-Tg(Alb-cre)21Mgn/J mice; AST, aspartate aminotransferase; BAT, brown adipose tissue; BMDM, bone marrow–derived macrophage; HFD, high-fat diet; KC, Kupffer cell; LPS, lipopolysaccharide; Lyzs, Cre, B6.129P2-Lyz2tm1(cre)Ifo/J; ND, normal chow diet; P/S, penicillin and streptomycin; PA, palmitate; PPARα, peroxisome proliferator-activated receptor-α; STAT, signal transducer and activator of transcription.

results. Our findings suggest that myeloid p38 has a dual role in inflammation and that drugs targeting IL-12 might improve the homeostatic regulation of energy balance in response to metabolic stress.

INTRODUCTION

Obesity is a global pandemic implicated in the development and progression of diabetes, cancer, and heart failure.[1] Obesity-related comorbidities are associated with low-grade inflammation.[1] This inflammation is systemic but prominently affects adipose tissue and the liver, which undergo increased infiltration by myeloid inflammatory cells like macrophages.[2]

Macrophage accumulation in these tissues is implicated in tissue inflammation and fibrosis, contributing to metabolic disease progression.[3] In addition to infiltrating macrophages, the liver in particular contains a robust population of resident macrophages, known as Kupffer cells (KCs). KCs represent 35% of all liver nonparenchymal cells and constitute the largest tissue population of resident macrophages in the body; there are 20–30 KCs for every 100 hepatocytes.[4] These resident macrophages appear to be critical for liver homeostasis,[5] contributing in healthy individuals to metabolism and the scavenging of bacteria and cell debris. However, obesity is associated with the dysregulation of resident KCs and their replacement by monocyte-derived macrophages.[6]

Myeloid cells such as macrophages can also alter the expression of the endocrine hormone Fibroblast growth factor 21 (FGF21).[7,8] The liver is the major source of this hepatokine, which regulates systemic metabolism through the activation of brown adipose tissue (BAT) thermogenesis and the transformation of white adipocytes to brown-like adipocytes, a process called browning.[9] Hepatic FGF21 expression is regulated via the nuclear receptor peroxisome proliferator-activated receptor-α (PPARα) in response to nutritional stresses such as fasting, ketogenic diet, or lipid overload.[10] In addition, a reciprocal interaction has recently been described between adipose tissue and hepatocytes, in which adiponectin released from fat controls hepatic FGF21 production.[11]

Macrophage production of proinflammatory cytokines is critically regulated by p38 mitogen activated protein kinase (MAPK),[12] and lack of several p38s in the myeloid compartment results in reduced cytokine production and protection against steatohepatitis.[13,14] The p38 protein family includes four isoforms, p38α, p38β, p38γ, and p38δ, which are activated by the upstream kinases mitogen activated protein kinase kinase (MKK)3 and MKK6.[1] All four isoforms are expressed in the myeloid compartment, and several of their functions have been defined. Macrophage deletion of p38α or p38γ/δ partially impairs the inflammatory response to lipopolysaccharide (LPS),

resulting in decreased production of LPS-induced cytokines.[12,15,16] Lack of myeloid p38α and p38γ/δ protects against acute liver damage due to the decreased macrophage inflammatory response.[12,17] Consistent with this proinflammatory role of the p38 pathway, lack of p38γ/δ in the myeloid compartment reduces the severity of diet-induced steatosis in mice.[14] In obesity, myeloid p38α contributes to M1 macrophage polarization and the production of proinflammatory cytokines, resulting in lipid accumulation in hepatocytes.[13] These findings suggest that deletion of p38 upstream kinases in myeloid cells could ameliorate obesity-induced metabolic disease.

Here, we report that activation of p38 in liver macrophages modulates liver FGF21 signaling to BAT, thereby promoting thermogenesis and protecting against diet-induced obesity. Although excessive p38 activation in liver macrophages has been reported to be deleterious and to promote hepatic steatosis,[13,14] we found that its physiological activation is necessary for correct interaction between hepatocytes and macrophages. This mechanism represents a signaling node in which macrophages contribute to liver homeostasis and the hepatic endocrine function, helping to preserve the correct whole-body metabolism.

METHODS

Study population

The human study population included liver biopsies from 44 individuals recruited among patients undergoing laparoscopic cholecystectomy for gallstone disease. The criteria applied in the histological analysis were as follows: for the hepatocyte ballooning study, we considered livers to be positive for ballonization if they presented from few to massive ballooned hepatocytes and containing or not Mallory's hyaline. Samples histology were considered positive for binucleation with the presence of one or more binucleated cells. We classified livers with severe steatosis those with more than 66% of steatotic surface area in the histological sample. The study was approved by the Ethics Committee of the University Hospital of Salamanca(Spain), ensuring that it conformed to the ethical guidelines of the 1975 Declaration of Helsinki, and all patients gave written informed consent. Patients were excluded if they had a history of alcohol use disorders or excessive alcohol consumption,

chronic hepatitis C or B, or a body mass index ≥35. Participant characteristics are listed in Table S1. All data and information of the human cohort were provided by University Hospital of Salamanca.

Animal models

Mice with a floxed mutation in the *Map2k6* (*Mkk6*) gene were as described.[18] Mice with a germ-line mutation in the *Map2k3* (*Mkk3*) gene and LoxP elements inserted into two introns (*Map2k3*LoxP) were generated after homologous recombination in embryonic stem (ES) cells, obtained from EUCOMM clon EPD0160_3_H09. The ES cell clones were injected into C57BL/6J blastocysts to create chimeric mice that transmitted the mutated *Map2k3* allele through the germ line. The Flp NeoR cassette was excised by crossing these mice with Actin beta: Flipase thermostable derivative (ACTB:FLPe) B6;SJL mice, which express an FLP1 recombinase gene under the direction of the human ACTB promoter (Figure S1A). These animals were crossed with B6.129P2-Lyz2tm1(cre) Ifo/J mice to generate mice lacking MKK3 and MKK6 specifically in myeloid cells (MKK3/6$^{Lyzs-Knockout (KO)}$) on the C57BL/6J background (Jackson Laboratory). B6.129P2-Lyz2tm1(cre)Ifo/J (Lyzs-Cre) and control littermates (MKK3/6$^{f/f}$) were used as controls. For the generation of FGF21^{Alb-KO} mice, the FGF21^{loxP} (B6.129S6[SJL]-Fgf21tm1.2Djm/J) line was crossed with B6.Cg-Tg(Alb-cre)21Mgn/J mice on the C57BL/6J background (Jackson laboratory). B6.Cg-Tg(Alb-cre)21Mgn/J mice (Alb-Cre) were used as controls. All mice were backcrossed for 10 generations to the C57BL/6J background (Jackson Laboratory). Genotypes were confirmed by polymerase chain reaction (PCR) analysis of genomic DNA. Radiation chimeras were generated by exposing FGF21^{Alb-KO} and Alb-Cre recipient mice to 2 cycles of ionizing radiation (625 Gy) and reconstituting them by tail-vein injection of $5 × 10^6$ donor bone marrow cells from MKK3/6$^{Lyzs-KO}$ or Lyzs-Cre mice. C57BL/6J wild-type mice were intraperitoneally injected with recombinant murine IL-12p70 (30 μg/kg) (PeproTech no. 210-12) for 6 h. Mice were cohoused under a 12 h light/12 h dark cycle in a specific pathogen-free facility. In all experiments, male mice between 8 and 12 weeks old were used. Mice were fed a normal chow diet (ND) (Altromin, no. 1410) or a high-fat diet (HFD) (Research Diets, no. D11103002i) for 8–10 weeks. To choose the size of the sample, we have used the 3R rule to ensure statistical validity and significance with the chosen size. Centro Nacional de Investigaciones Cardiovasculares (CNIC) has biostatisticians to help in designing our animal experiments. They use the most update statistical methods to ensure that the correct number of animals will be employed in each experiment. The number of animals in each group is determined by the statistical power that is required to detect significant biologically relevant differences. We used 6–14 mice per group for at least 80% power for one- and two-sided testing. Animals that presented disease or had been bitten because of a fight in the cage were excluded. All animal procedures were approved by the Animal Care and Use Committee at CNIC conformed to EU Directive 86/609/EEC and Recommendation 2007/526/EC regarding the protection of animals used for experimental and other scientific purposes, enacted under Spanish law 1201/2005. The protocol code is PROEX 215/18.

Cell culture and cell lines

The wild-type immortalized mouse hepatocyte cell line was generated by transformation of primary neonate hepatocytes from C57BL/6J male mice with simian virus 40 (SV40 virus) containing an antibiotic-resistance plasmid (neomycin, puromycin). These cells were cultured in Dulbecco's Modified Eagle Medium with 10% fetal bovine serum (FBS) (Gibco, no. 1027–106), penicillin and streptomycin (P/S) (Sigma-Aldrich, no. P4333) and 1% L-glutamine (Hy0043lone, no. SH30034.01). L929 cells were cultured in Roswell Park Memorial Institute medium +10%FBS + 1%P/S + 1% L-glutamine. Supernatants as a source of macrophage colony-stimulating factor were collected after 2 days of culture. The human liver cell line THLE-2 was cultured as previously described.[19]

All cell lines and cell cultures were grown at 37°C in a 5% CO_2 humid atmosphere.

Isolation of bone marrow–derived macrophages

Bone marrow–derived macrophages (BMDMs) were generated by flushing the hind limbs of MKK3/6$^{Lyzs-KO}$ or Lyzs-Cre mice with phosphate-buffered saline (PBS) + P/S. The bone marrow cells were cultured overnight in p250 Petri dishes in DMEM +10% FBS, P/S, and 20% L929-cell supernatant (used as a source of M-CSF). The next day, $4 × 10^6$ nonadherent cells were plated in p100 Petri dishes. After 3 days, the medium was replaced with fresh DMEM containing 10% inactivated FBS, P/S, and 20% L929 supernatant. After a total of 7 days of cell culture, cells were considered fully differentiated. One day before in vitro treatment, cells were serum-deprived overnight with DMEM containing 1% FBS and P/S.

In vitro macrophage stimulation

BMDMs were treated with 0.1 mM palmitate (PA) (Sigma-Aldrich, no. P0500) for 6 h and then stimulated with LPS (100 ng/mL, Sigma-Aldrich no. L4130) for 8, 12, 16, 24, or 36 h. Culture supernatants were collected and stored at −80°C for subsequent experiments. Cells were frozen for RNA isolation and quantitative (q) PCR analysis.

In vitro mouse hepatocyte treatment

One day before stimulation, 40×10^4 immortalized wild-type mouse hepatocytes were plated per well of a 12-well plate in DMEM containing 10% FBS, P/S, and 1% L-glutamine. The next day, the medium was changed to DMEM containing 0.5% FBS, P/S, and 0.5 mM PA. After 6 h, depending on the experiment, cells were exposed to IL-12p70 (10 ng/mL, PeproTech no. 210–12) for 6, 12, or 24 h or to macrophage culture supernatant for 6 or 24 h. In some experiments macrophages culture supernatant were incubated with anti–IL-12 neutralizing antibody (1 μg/mL, Abcam no. ab80682) or IgG isotype (1 μg/mL, Sigma-Aldrich no. I8140). Cells were frozen for RNA isolation and qPCR analysis.

In vitro THLE-2 cells treatment

A total of 30×10^4 THLE-2 cells were plated per well of a 6-well plate in Bronchial Epithelial cell Basal Medium (Lonza, no. CC-3170) with 10% FBS. The day of the stimulation, cells were treated first with 0.5 mM PA for 6 h and then exposed to IL-12p70 (10 ng/mL) for another 6 h. Cells were frozen for RNA isolation and qPCR analysis.

Cytokine ELISA

Cytokines were measured in macrophage culture supernatants by multiplexed enzyme-linked immunoassay using a mouse cytokine kit (Invitrogen, no. LMC0006M) and a Luminex 200 analyzer (MilliporeSigma).

Tissue digestion for flow cytometry

For the isolation of liver leukocytes, mice were perfused with 20 ml PBS, and livers were collected, dissociated, and digested at 37°C for 30 min with 0.5 mg/mL collagenase A (Roche, no. 10103586001) and 2 U/mL DNase (Sigma-Aldrich, no. D4513). For cell sorting, livers were perfused using a peristaltic pump with 30 ml modified Hanks balanced salt solution (without $MgCl_2$ or $CaCl_2$ and containing 1 M Hepes and 0.1 M EGTA) and 25 ml of 0.8 mg/mL collagenase type I (Worthington Biochemical Corp., no. LS004197). Livers were collected as a cell suspension in complete DMEM (containing 10% FBS, 40% F-12, 0.2 mg/mL BSA, sodium pyruvate, 0.01 M Hepes, 1% L-glutamate, P/S, and 0.51 mg/mL $NaHCO_3$). The cell suspension was passed through a 70-μm strainer and centrifuged twice at 500 rpm for 2 min to remove the liver parenchyma. BAT was also collected and carefully excised, minced, and digested with 1 mg/mL liberase TL (Sigma-Aldrich, no. 5401020001) and 2 U/mL DNAse for 30 min at 37°C

with shaking. The cell suspension was then passed through a 70-μm strainer and centrifuged at 1500 rpm. In all tissue samples, pelleted erythrocytes were lysed with a red-cell lysis buffer (NH_4Cl, $NaHCO_3$, 20 mM EDTA), and leukocytes were subsequently resuspended in flow cytometry buffer (PBS containing 1% FBS and 5 mM EDTA).

Flow cytometry analysis and cell sorting

Single-cell suspensions were stained with the following surface-marker antibodies: anti-CD45 V450 (30-F11), anti-CD11b fluorescein isothiocyanate (FITC) (M1/70), anti-F4/80 phycoerythrin (PE)-Cy7 (BM8) or Alexa 647 (Cl: A3-1), goat anti-Clec4F (polyclonal) conjugated to anti-goat Alexa 647, anti-Tim4 PE (RMT4-54), anti-CD206 BV711 (MMR), and anti-CD11c PE (HL3). Dead cells were excluded by (4',6-diamidino-2-fenilindol) DAPI staining. Cells were sorted in a FACSAria cell sorter to >95% purity. Flow cytometry experiments were performed in a BD LSRFortessa cell analyzer, and data were analyzed with FlowJo software. Detailed information of antibodies is listed in Table S2.

Adenoviral vector production

The adeno-associated virus (AAV) shuttle and helper plasmids were transfected into HEK 293A cells by calcium-phosphate coprecipitation. A total of 840 μg plasmid DNA (mixed in an equimolar ratio) was used per HYPERFlask (Corning) seeded with 1.2×10^8 cells the day before. Seventy-two hours after transfection, the cells were collected by centrifugation and the cell pellet was resuspended in 50 mM Tris HCl, 150 mM NaCl, 2 mM MgCl2 buffer on ice before digestion with DNase I and RNaseA (0.1 mg/mL: 1 each; Roche) at 37°C for 60 min. Clarified supernatant containing the viral particles was obtained by iodixanol gradient centrifugation. Gradient fractions containing virus were concentrated using Amicon UltraCel columns (MilliporeSigma) and stored at −70°C.[20] Recombinant AAV9 expressing mouse FGF21 or green fluorescent protein (GFP) were titered and 1×10^{11} virus particles per mouse in PBS expressing were intravenously injected into mice through the tail vein.

Immunoblotting

Samples were lysed with lysis buffer containing protease and phosphatase inhibitors (50 mM Tris [pH 7.5], 1%Triton X-100, 1 mM EDTA, 1 mM EGTA, 50 mM NaF, 1 mM Na-β-glycerophosphate, 5 mM Na pyrophosphate, 1 mM Na orthovanadate, 0.27 M sucrose, 0.1 mM phenylmethylsulfonyl fluoride, 1 mM β-mercaptoethanol,

10 μg/mL aprotinin, and 5 μg/mL leupeptin). Lysates were separated by sodium dodecyl sulfate polyacrylamide gel electrophoresis and transferred to nitrocellulose membranes, and the membranes were incubated with the antibodies listed in Table S2. Primary and secondary antibodies were used at 1:1000 and 1:5000 dilutions, respectively. Immunocomplexes were detected by enhanced chemiluminescence (Amersham, no. RPN2232) and analyzed with ImageJ software.

qPCR analysis

Total RNA was extracted with the RNeasy Plus Mini kit or RNeasy Plus Micro kit (Quiagen, no. 74106 or no. 217084). RNA was then transcribed to complementary DNA (Applied Biosystems, no. 4368814), and Real Time (RT)-qPCR was performed using Fast SYBR Green probe (Applied Biosystems, no. 4385616) and appropriate primers in a 7900 Fast Real Time thermocycler (Applied Biosystems). Human *IL12B* was measured with a Taqman probe from Thermo Fisher Scientific. Primers and Taqman probe are listed in Table S3.

Histology

Liver and BAT samples were fixed in 10% formalin for 48 h, dehydrated, and embedded in paraffin. Sections (5 μm) were cut and stained with hematoxylin and eosin (Sigma-Aldrich, no. H3136 and Thermo Fisher Scientific, no. 6766008). Sections were examined with a Leica DM2500 microscope fitted with a 20× objective.

UCP1 immunostaining

BAT was fixed with formalin 10%, included in paraffin, cut into 5-μm sections, and sequentially stained with anti-uncoupling protein 1 (UCP1) antibody (1/500, Abcam no. AB10983), biotinylated goat anti-rabbit secondary antibody (1/500, Jackson ImmunoResearch Laboratories no. 111–066-003), streptavidin-conjugated avidin-biotin complex (Vector Laboratories, no. PK-6100), and the substrate 3,3′-diaminobenzidene conjugated to horseradish peroxidase (Vector Laboratories, no. SK-4100). Sections were then briefly counterstained with Nuclear Fast Red (Sigma-Aldrich, no. N-3020).

Glucose tolerance test

Overnight-fasted mice received an intraperitoneal injection of glucose (1 g/kg body weight), and blood glucose levels were quantified with Contour Next One glucometer (Ascensia Diabetes Care) at 0, 15, 30, 60, 90, and 120 min postinjection.

Insulin tolerance test

One hour–fasted mice received an intraperitoneal injection of 0.75 IU/kg insulin (Eli Lilly & Co), and blood glucose levels were measured with the glucose meter at 0, 15, 30, 60, and 90 min postinjection.

Indirect calorimetry system

Energy expenditure, respiratory exchange, locomotor activity, and food intake were quantified using the indirect calorimetry system (TSE LabMaster, TSE Systems) over 3 days.

BAT temperature

BAT-adjacent interscapular temperature was quantified by thermographic imaging using a FLIR T430sc Infrared Camera (FLIR Systems, Inc., Wilsonville, Oregon) and FLIR software.

Magnetic resonance imaging and nuclear magnetic resonance spectroscopy

Body fat and lean mass were quantified by nuclear magnetic resonance imaging using a Whole-Body Composition Analyzer (EchoMRI, Houston, Texas) and ImageJ software.

Determination of mouse alanine aminotransferase and aspartate aminotransferase in serum

Serum activities of alanine aminotransferase (ALT) and aspartate aminotransferase (AST) in mice were measured with ALT and AST reagent kits (SpinReact no. 41282 and Biosystems Reagents no. 11531, respectively) in a Benchmark Plus microplate spectrophotometer.

Statistics

Data are expressed as means ± SEMs. Two-group comparisons were analyzed by two-tailed Student t test, and multiple group comparisons were analyzed by one-way or two-way analysis of variance coupled with the Tukey or Bonferroni multigroup test, respectively. When variances were different, two and multiple groups were tested applying Welch's test correction and Kruskal-Wallis test coupled to Dunn's multiple test, respectively. For all tests, differences were considered significant at a two-sided $p < 0.05$. All analyses were performed using Excel (Microsoft Corp.) and GraphPad PRISM 8 software.

Details of statistical comparisons are indicated in the figure legends.

RESULTS

Activation of p38 in myeloid cells protects against diet-induced obesity through the activation of thermogenesis

To elucidate the role of myeloid p38 in obesity, we generated MKK3/6$^{Lyzs-KO}$ mice, which lack the *Mapk2k3* and *Mapk2k6* genes encoding the MKK3 and MKK6 upstream activators of the p38 pathway specifically in myeloid cells and used as control mice Lyzs-Cre mice and MKK3/6$^{f/f}$ littermates. Immunoblot analysis of MKK3/6$^{Lyzs-KO}$ and control mice confirmed MKK3 and MKK6 deletion in MKK3/6$^{Lyzs-KO}$ macrophages and KCs but not in MKK3/6$^{Lyzs-KO}$ liver, BAT, epididymal white adipose tissue, or subcutaneous white adipose tissue (Figure 1A, Figure S1B). Mice were fed an ND or HFD for 10 weeks. Mice fed the ND showed no differences in body weight or glucose metabolism parameters (blood glucose, insulin sensitivity, and glucose tolerance) (Figure S1C,D). In contrast, after 10 weeks on the HFD, MKK3/6$^{Lyzs-KO}$ mice had higher body weight and adipose tissue mass than Lyzs-Cre or MKK3/6$^{f/f}$ mice with no difference in food intake (Figure 1B,C, Figure S2A,B). Indirect calorimetry analysis demonstrated that MKK3/6 deficiency in myeloid cells decreased VO_2, VCO_2, and energy expenditure in HFD-fed mice, but there were no differences in the respiratory exchange ratio (RQ) between genotypes (Figure 1D, Figure S2A,B). MKK3/6$^{Lyzs-KO}$, Lyzs-Cre and MKK3/6$^{f/f}$ mice showed no differences in ambulatory and vertical movement on the HFD, indicating that the decrease in energy expenditure in the MKK3/6$^{Lyzs-KO}$ mice was not due to reduced locomotor activity (Figure S2A,B). In contrast, HFD-fed MKK3/6$^{Lyzs-KO}$ mice showed a reduction in BAT temperature in comparison with Lyzs-Cre or MKK3/6$^{f/f}$ mice that was not observed on the ND (Figure 1E, Figures S1E and S2B). Analysis of BAT sections revealed morphological evidence of increased adiposity and decreased UCP1 content in HFD-fed MKK3/6$^{Lyzs-KO}$ mice, a finding confirmed by western blot (Figure 1F,G, Figure S2B). Indeed, expression of genes related to thermogenesis was decreased in the BAT of HFD-fed MKK3/6$^{Lyzs-KO}$ mice (Figure 1H).

Activation of p38 in myeloid cells protects against obesity-induced diabetes, insulin resistance, and liver steatosis

Decreased energy expenditure and increased body weight are associated with a deleterious metabolic phenotype. In concordance, HFD-fed MKK3/6$^{Lyzs-KO}$ mice had higher plasma glucose, more severe glucose intolerance, and higher insulin resistance than Lyzs-Cre mice on the same diet (Figure 2A). HFD-fed MKK3/6$^{Lyzs-KO}$ mice also developed more aggressive liver steatosis, correlating with elevated expression of lipogenesis-related genes (*Acaca*, *Srebpc1*, and *Fasn*) (Figure 2B,C). In agreement with observed insulin resistance (Figure 2A), myeloid MKK3/6 deficiency blunted the increase in liver AKT phosphorylation in response to the HFD, indicating reduced responsiveness of MKK3/6^{LyzsKO} liver to insulin stimulation (Figure 2D).

Activation of p38 in myeloid cells does not affect BAT macrophages populations

Examination of BAT CD11b$^+$ F4/80$^+$ cells in MKK3/6$^{Lyzs-KO}$ and Lyzs-Cre mice revealed no differences in macrophage cell number in mice fed with either the ND or the HFD (Figure 3A, Figure S3A). We next examined surface marker expression in these BAT macrophages from MKK3/6$^{Lyzs-KO}$ and Lyzs-Cre mice to determine the relative proportion of CD11c$^+$CD206$^-$ cells, implicated in development of insulin resistance,[21] and CD11c$^-$CD206$^+$ cells, which promote thermogenesis.[22] Flow cytometry analysis detected no between-genotype differences in the numbers of CD11c$^+$ CD206$^-$ and CD11c$^-$ CD206$^+$ BAT macrophages (Figure 3A, Figure S3A).

The whole-body effect of deficient myeloid p38 activation is mediated by impaired endocrine signaling by hepatic FGF21

Hepatic FGF21 has been reported to increase energy expenditure by promoting thermogenesis.[9,10,23] We found that HFD-fed MKK3/6$^{Lyzs-KO}$ mice had lower mRNA expression of hepatic *Fgf21*, a lower liver content of FGF21 protein, and decreased levels of circulating FGF21 comparing to control mice (Figure 3B,C and Figure S3B).

To assess whether inhibition of hepatic FGF21 is responsible for the obese phenotype, impaired BAT thermogenesis, and energy expenditure in HFD-fed MKK3/6^{LyzsKO} mice, we generated mice lacking FGF21 in liver (FGF21^{Alb-KO}) together with their corresponding control mice (Alb-Cre). Using these mice as recipients, we performed bone marrow transplantation experiments with MKK3/6$^{Lyzs-KO}$ or Lyzs-Cre mice as donors, followed by HFD feeding (Figure 3D). In experiments with Alb-Cre recipients (with intact hepatic FGF21 production) mice receiving MKK3/6$^{Lyzs-KO}$ bone marrow (MKK3/6$^{Lyzs-KO}$ > Alb-Cre) increased body weight more on the HFD than those receiving Lyzs-Cre bone marrow (Lyzs-Cre > Alb-Cre)
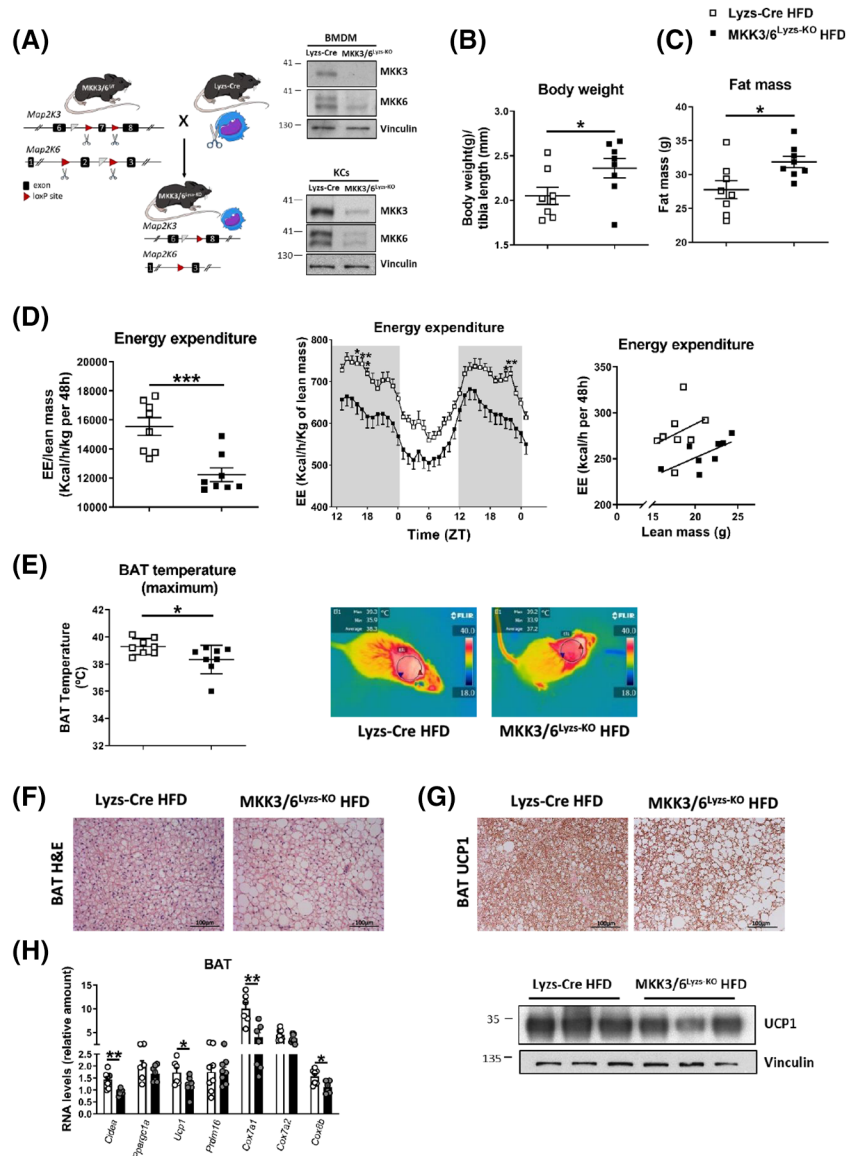
FIGURE 1 MKK3 and MKK6 deficiency in myeloid cells promotes obesity and alters brown adipose tissue (BAT) thermogenesis and energy expenditure after high-fat diet (HFD) feeding. (A) Knock-out strategy for specific deletion of mitogen activated protein kinase kinase 3 (*Mkk3*) (*Map2k3*) and Mkk6 (*Map2k6*) encoding genes in myeloid cells. Immunoblot showing deletion of MKK3 and MKK6 proteins in bone marrow–derived macrophages (BMDMs) and Kupffer cells (KCs). (B–H) Lyzs-Cre and MKK3/6$^{Lyzs-KO}$ mice were fed an HFD for 10 weeks, and distinct metabolic parameters were determined: (B) body weight normalized by tibia length; (C) nuclear magnetic resonance analysis of fat mass; (D) energy expenditure (EE) analysis in metabolic cages over a 2-day period after 6 weeks of HFD. From left to right panels, EE is expressed as accumulative, hour by hour, and as analysis of covariance analysis. EE values are corrected by lean mass; (E) skin temperature surrounding interscapular brown adipose tissue (BAT). (*n* = 8 mice per group). Right panels show representative infrared thermal images; (F) representative hematoxylin-eosin stain of BAT; (G) immunohistochemistry staining (upper panel) and immunoblot analysis of UCP1 protein content in BAT (lower panel) (Scale bar: 100 μm); and (H) mRNA levels of thermogenic genes (relative to *Gapdh*) in BAT. (*n* = 6–8 mice per group). Data are means ± SEM. *$p < 0.05$, **$p < 0.01$, ***$p < 0.001$ by Student *t* test (B, C, D left panel, E, H) or two-way analysis of variance coupled to Bonferroni's multiple test (D, medium panel).

(Figure 3E). MKK3/6$^{Lyzs-KO}$ > Alb-Cre and Lyzs-Cre > Alb-Cre mice presented no differences in food intake (Figure S3C). In contrast, hepatic FGF21-deficient recipients of MKK3/6$^{Lyzs-KO}$ and Lyzs-Cre bone marrow (MKK3/6$^{Lyzs-KO}$ > FGF21^{Alb-KO} and Lyzs-Cre > FGF21^{Alb-KO}) showed no differences in body weight (Figure 3E). Consistent with these results, transfer of MKK3/6$^{Lyzs-KO}$ bone marrow reduced energy expenditure only in recipient mice with intact hepatic FGF21 production (Figure 3F), without affecting RQ (Figure S3C). These changes in energy expenditure were not caused by fluctuations in locomotor activity (Figure S3C). The effect of myeloid MKK3/6 deficiency on glucose homeostasis was also only evident in mice with intact hepatic FGF21 production, because these parameters were impaired in FGF21^{Alb-KO} mice
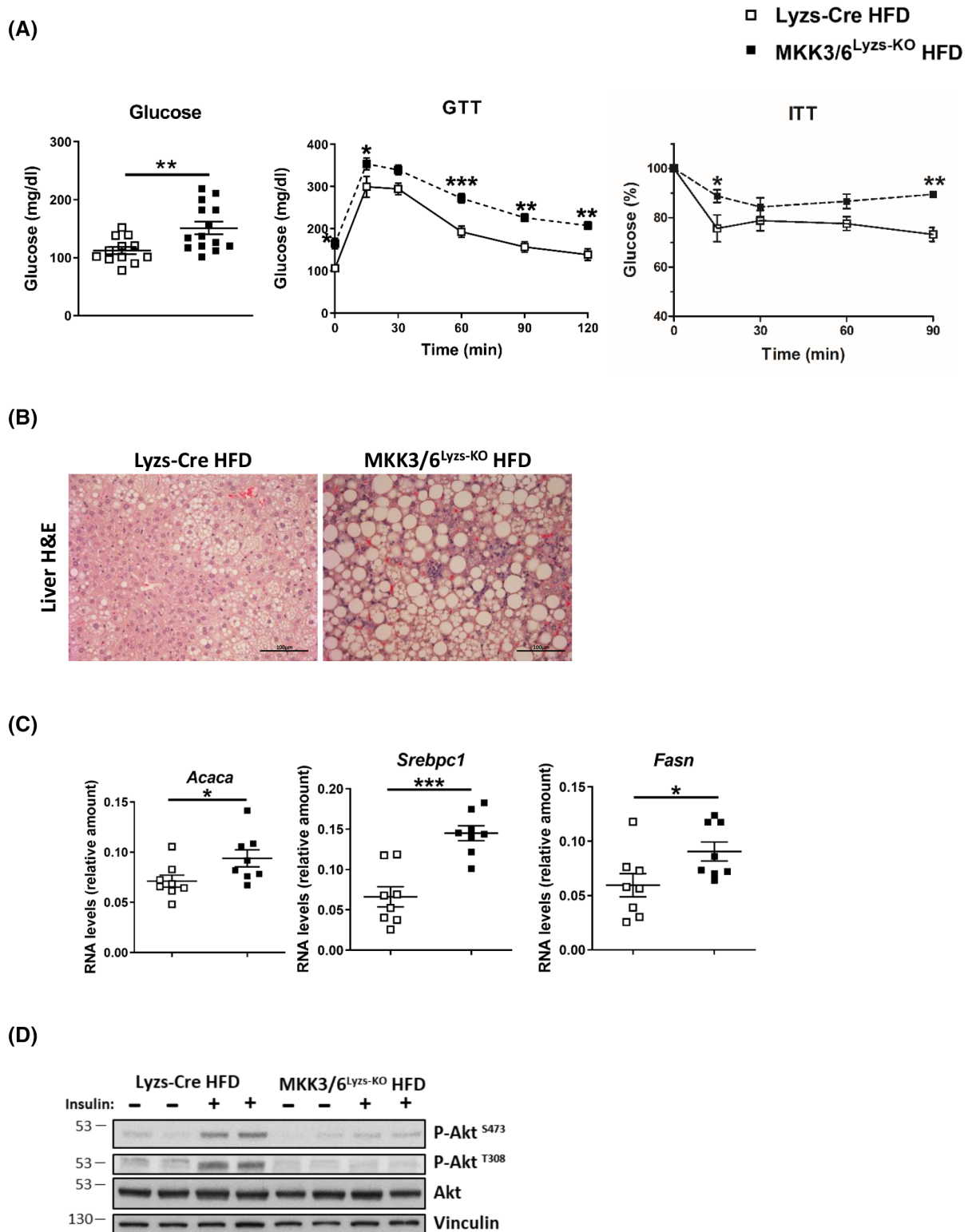
(A)

(B)

(C)

(D)

FIGURE 2 MKK3 and MKK6 deficiency in myeloid cells alters glucose metabolism and promotes steatosis and insulin resistance in the liver after high-fat diet (HFD) feeding. (A) Glucose metabolism was determined after 8 weeks of HFD in Lyzs-Cre and MKK3/6$^{Lyzs-KO}$ mice. From left to right, figure shows fasting glucose levels (n = 12–14 mice per group), glucose tolerance test (GTT), and insulin tolerance test (ITT). (*n* = 10 mice per group). (B–D) Livers from Lyzs-Cre and MKK3/6$^{Lyzs-KO}$ after 10 weeks of HFD were analyzed: (B) representative hematoxylin-eosin stain (H&E) of livers (scale bar: 100 μm); (C) mRNA levels of genes related to lipogenesis pathway (relative to *Gapdh*). (*n* = 8 mice per group); (D) analysis of insulin pathway activation by immunoblot determination of phospho-Akt levels in livers before (−) or after 15 min of insulin intraperitoneal injection (+). Data are means ± SEM. *$p < 0.05$, **$p < 0.01$, ***$p < 0.001$ by Student *t* test (A left panel, C) or two-way ANOVA coupled to Bonferroni's multiple test (A medium and right panels).
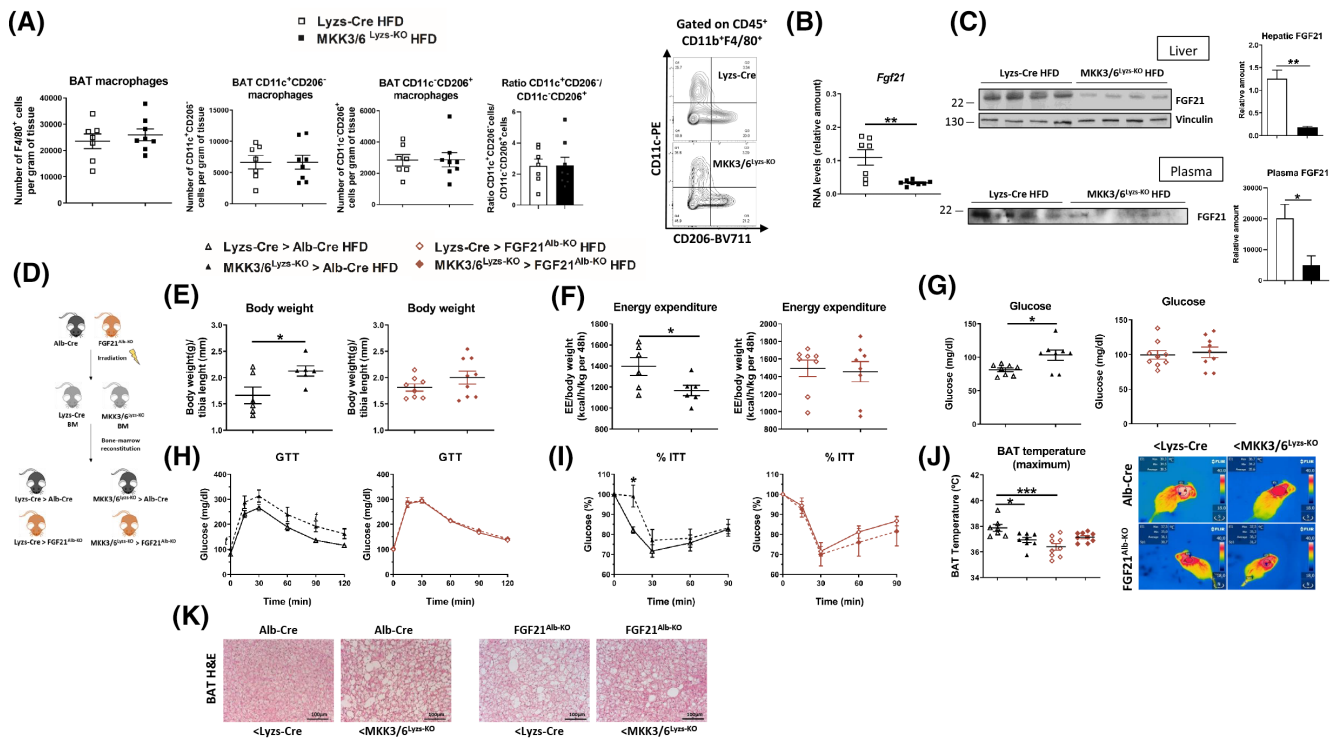
FIGURE 3 Lack of myeloid MKK3/6 affects whole-body metabolism through hepatic Fibroblast Growth Factor 21 (FGF21) after high-fat diet (HFD) feeding. (A–C) Lyzs-Cre and MKK3/6$^{Lyzs-KO}$ mice were fed an HFD for 10 weeks and BAT was analyzed: (A) From left to right, CD45$^+$, CD11b$^+$, F4/80$^+$ cells (total BAT-associated macrophages), CD45$^+$, CD11b$^+$, F4/80$^+$ CD11c$^+$CD206$^-$ cells and CD45$^+$, CD11b$^+$, F4/80$^+$ CD11c$^-$CD206$^+$ cells in the stromal vascular fraction from BAT determined by flow cytometry. Ratio of CD11c$^+$CD206$^-$/ CD11c$^-$CD206$^+$ is shown. (n = 7–8 mice per group). Representative plots showing BAT-associated macrophage populations are shown on the right; (B) mRNA levels of hepatic *Fgf21* (relative to *Gapdh*) (n = 7–8 mice per group) and (C) immunoblot analysis of hepatic and circulating FGF21 levels in Lyzs-Cre and MKK3/6$^{Lyzs-KO}$ mice after HFD. Immunoblot quantification is shown in left panels. (D–K) Chimeric mice were generated by bone marrow (BM) transplantation of Lyzs-Cre or MKK3/6$^{Lyzs-KO}$ BM in Alb-Cre and FGF21^{Alb-KO} recipients. After 8 wk of reconstitution, mice were fed an HFD for 18 wk and distinct metabolic parameters determined: (D) experimental scheme for the generation of chimeric mice by bone marrow transplantation; (E) body weight normalized by tibia length; (F) Energy expenditure (EE) analysis of HFD-fed mice in metabolic cages over a 2-day period after 16 weeks of HFD; (G) fasting glucose levels; (H) glucose tolerance test (GTT); (I) insulin tolerance test (ITT); (J) skin temperature surrounding interscapular BAT of the indicated recipients. (n = 6–8 mice per group). Right panels show representative infrared thermal images; and (K) representative hematoxylin-eosin stain of BAT (Scale bar: 100 μm). Data are means ± SEM. *$p < 0.05$, **$p < 0.01$, ***$p < 0.001$ by Student t test (A–G), two-way analysis of variance coupled to Bonferroni's multiple test (H,I) or one-way ANOVA coupled to Tukey's multiple test (J); t ($p < 0.05$) by Student t test (H).

in the absence of MKK3/6-deficient myeloid cells, and MKK3/6$^{Lyzs-KO}$ bone marrow to these mice had no further effect (Figure 3G–I). Moreover, although MKK3/6$^{Lyzs-KO}$ bone marrow transfer resulted in a lower BAT temperature in Alb-Cre recipients, this effect was not seen in FGF21^{Alb-KO} recipients, in which BAT temperature was similarly lower than in Alb-Cre mice irrespective of which bone marrow population was transferred (MKK3/6$^{Lyzs-KO}$ or Lyzs-Cre) (Figure 3J). Histological analysis demonstrated that lack of hepatic FGF21 due to genetic modification (FGF21^{Alb-KO} mice) or disrupted communication between liver macrophages and hepatocytes (MKK3/6$^{Lyzs-KO}$ mice) resulted in BAT whitening (Figure 3K), indicating that hepatic FGF21 is required for protection against BAT whitening and the maintenance of thermogenesis during obesity.

To further corroborate the role of hepatic FGF21 in the phenotype of mice lacking myeloid p38 activation,

we overexpressed FGF21 in the livers of MKK3/6$^{Lyzs-KO}$ mice using AAV-FGF21 infection, followed by a HFD. As controls, we infected myeloid-KO and control mice with AAV-GFP (Figure S4A). Fourteen days postinfection, we verified the expression of circulating FGF21 in plasma of infected mice (Figure S4B). After HFD feeding, as expected, MKK3/6$^{Lyzs-KO}$ mice infected with the control virus presented higher body weight comparing to controls (Figure S4C), reproducing the phenotype previously observed (Figure 1 and Figure S2B). In contrast, when hepatic FGF21 was induced in MKK3/6 myeloid-KO mice, body weight was significantly reduced comparing to all experimental groups (Figure S4C). In line with this result, the decreased in energy expenditure and BAT temperature found in MKK3/6$^{Lyzs-KO}$-AAV-GFP mice comparing to controls, was reverted after hepatic FGF21 overexpression (Figure S4D,E).

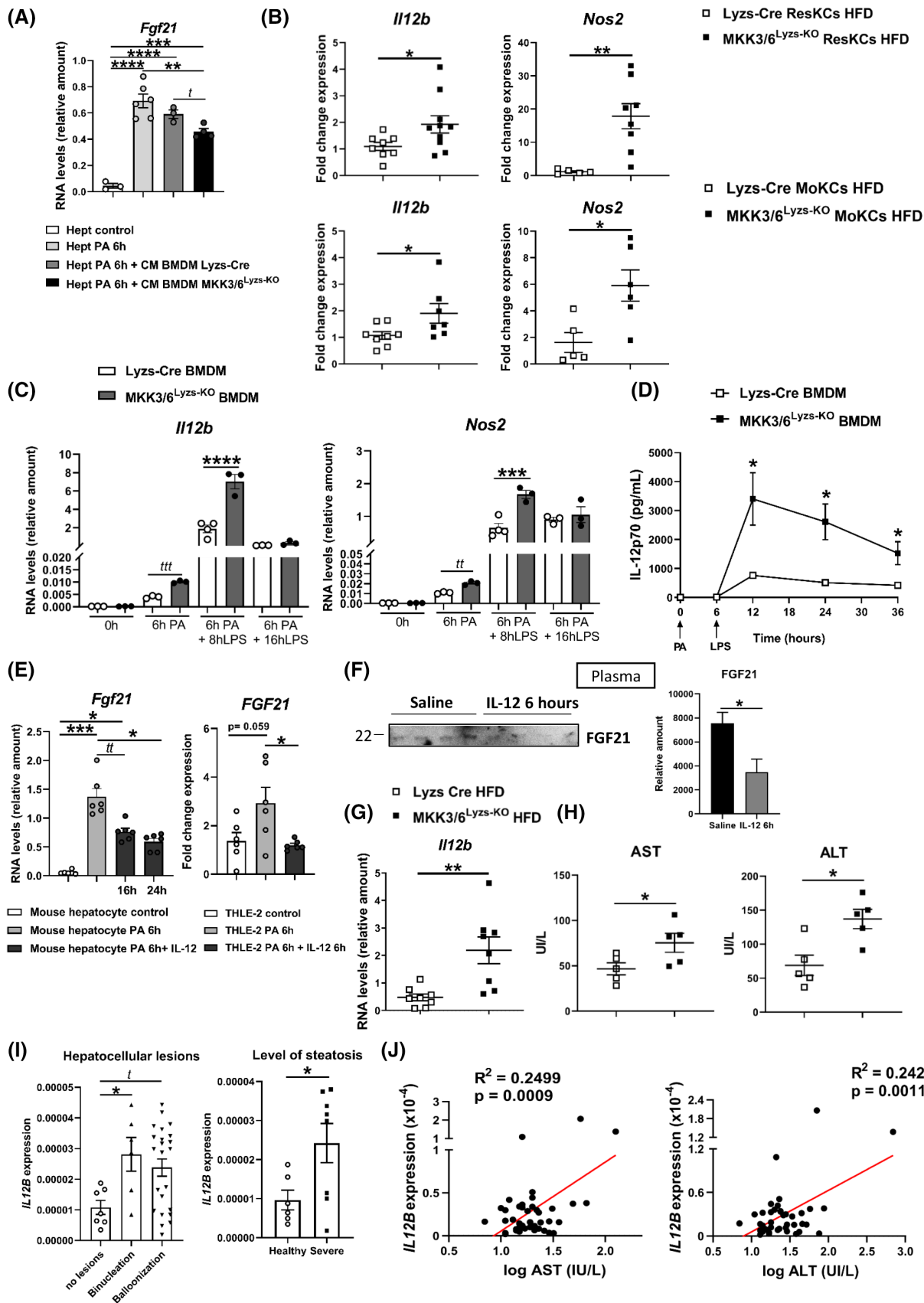## Liver-infiltrating macrophages control hepatic FGF21 production

KCs have been reported to regulate hepatocyte FGF21 expression through cytokine secretion.[8] To assess macrophage-to-hepatocyte communication under steatotic conditions, we first exposed hepatocytes to PA and then stimulated them with conditioned medium from MKK3/6[LyzsKO] or Lyzs-Cre macrophage cultures. Conditioned medium from both types of macrophages reduced hepatocyte *Fgf21* expression (Figure 4A), but the effect was stronger with medium from MKK3/6[Lyzs-KO] macrophages, suggesting that these cells secrete an inhibitor of FGF21 expression (Figure 4A). During HFD feeding, KCs are replaced by monocyte-derived macrophages.[24] Analysis of sorted resident macrophages (CLEC4F+ TIM4+) and monocyte-derived macrophages (CLEC4F+ TIM4−) from HFD-fed mice revealed higher expression of *Il12b* and *Nos2* mRNA in both liver macrophage populations from MKK3/6[Lyzs-KO] mice than in the counterpart Lyzs-Cre populations (Figure 4B). No significant differences were detected in the expression of other cytokines tested (Figure S5A). To mimic obesogenic and inflammatory conditions in vitro, we stimulated BMDM with LPS and PA. This treatment strongly stimulated *Il12b* and *Nos2* mRNA expression in MKK3/6-deficient BMDMs (Figure 4C) without inducing significant differences in the expression of other cytokines (Figure S5B). Analysis of conditioned medium revealed that LPS and PA induced the release of several cytokines by BMDMs of both genotypes (Figure S5C); however, increased IL-12p70 secretion was specific to MKK3/6[Lyzs-KO] BMDMs (Figure 4D). Interestingly, treatment of both, mouse hepatocytes and human THLE-2 hepatocytes with recombinant IL-12 reduced *Fgf21* expression (Figure 4E) and FGF21 protein levels (Figure S6A) suggesting that macrophage-derived IL-12 might

control liver FGF21 production. Indeed, IL-12 neutralization blunted the inhibitory activity of conditioned medium from MKK3/6[LyzsKO] BMDM on the hepatic *Fgf21* expression (Figure S6B). To physiologically demonstrate that IL-12 inhibits FGF21, we injected mice with recombinant mouse IL-12p70 and evaluated the FGF21 expression. After 6 h of IL-12 injection circulating FGF21 is reduced, indicating that IL-12 is able to inhibit its expression in vivo (Figure 4F).

To study the signaling pathways through which IL-12 could downregulate hepatic *Fgf21*, we first analyzed liver expression of IL-12 receptor subunits (*Il-12rb1* and *Il-12rb2*) and found that both of them were expressed by hepatocytes (Figure S6C). Then, we determined the activation state of IL-12 canonical pathway, the signal transducer and activator of transcription (STAT) pathway.[25] As shown in Figure S6D, IL-12 treatment on hepatocytes increased the phosphorylation of STAT5 and STAT3, indicating an activation of this signaling. PPARα is the main activator of *Fgf21* in the liver[26] and can be repressed by activated STATs.[27] In line with this, we also found that the expression of other common PPARα target genes was reduced after IL-12 exposure on hepatocytes (Figure S6E). Besides, we did not find differences in the level of phosphorylation of cJun NH2-terminal kinase, the negative regulator of PPARα in the liver[10] (Figure S6D). All these data indicate that IL-12 might modulate hepatic *Fgf21* by the repression of PPARα through STAT activation.

Collectively, these results strongly suggest that infiltrating inflammatory macrophages during obesity would induce IL-12 production and that p38 dysregulation exacerbate this process, leading to liver damage and reduced FGF21 production. Supporting this conclusion, HFD-fed MKK3/6[Lyzs-KO] mice showed increased expression of *Il12b* in the liver and increased circulating levels of the liver damage markers AST and ALT

FIGURE 4   IL-12 secreted by liver macrophages modulates hepatic *Fgf21* expression and correlates with liver damage in humans. (A) mRNA levels of *Fgf21* (relative to *Gapdh*) in cultured mouse hepatocytes treated 6 h with 0.5 mM palmitate (PA) and then 6 h with conditioned medium (CM) from Lyzs-Cre and MKK3/6[Lyzs-KO] BMDM (n = 3–6 wells per group). (B) Lyzs-Cre and MKK3/6[Lyzs-KO] mice were fed a HFD for 10 weeks, and ResKCs and MoKCs were FACS-sorted and purified from livers following the gating strategy indicated in Figure S4A. mRNA levels of *Il12b* and *Nos2* were determined by Real Time quantitative PCR (RT-qPCR) (relative to *Gapdh*) in both populations of liver macrophages. Resident Kupffer cells (ResKCs) and monocyted-derived Kupffer cells (MoKCs) are shown in the upper and lower panels, respectively (n = 5–10 pools of 2 mice per group from 3 different experiments). (C–D) BMDM differentiated from Lyzs-Cre and MKK3/6[Lyzs-KO] bone marrows were treated 6 h with 0.1 mM PA and then with LPS (100 ng/mL) at different times: (C) mRNA levels of *Il12b* and *Nos2* genes (relative to *Gapdh*) in BMDM (n = 3–4 wells per group); (D) levels of IL-12p70 in supernatants from BMDM (n = 4 pools of 2 mice per group). (E) mRNA levels of *Fgf21* (relative to *Gapdh*) in cultured mouse hepatocytes (left) or mRNA levels of *FGF21* (relative to *HPRT*) in human THLE-2 cells (right) treated 6 h with 0.5 mM palmitate (PA) and then with recombinant IL-12p70 (10 ng/mL) at the indicated time points. (n = 6 wells per group). (F) Immunoblot analysis of circulating FGF21 levels in wild-type mice 6 h after injection with saline or recombinant mouse IL-12p70 (30 μg/kg). Immunoblot quantification is shown in the right panel (n = 4 mice per group). (G) mRNA levels of *Il12b* (relative to *Gapdh*) in livers from in Lyzs-Cre and MKK3/6[Lyzs-KO] mice after HFD (n = 8 mice per group). (H) Serum levels of AST and ALT in Lyzs-Cre and MKK3/6[Lyzs-KO] mice after HFD (n = 5 mice/group). (I) Determination of *IL12B* mRNA expression (relative to *GAPDH*) in liver biopsies from a human cohort of patients classified according to the grade of hepatocellular lesions (left panel); and level of steatosis (right panel) where the healthy group correspond to patients without obesity or liver steatosis and the severe group are patients with obesity and massive steatosis (n = 36). (J) Correlation between mRNA levels of *IL12B* in human livers and AST (R^2 = 0.243; p = 0.0009) and ALT (R^2 = 0.243; p = 0.0011) serum concentration in those same individuals. Linear relationships between variables were tested using Pearson's correlation coefficient (n = 41). Data are means ± SEM. *p < 0.05, **p < 0.01 ***p < 0.001, ****p < 0.0001 by Student t test or Welch's test (B, D, E right panel, F-H, I right panel), one-way ANOVA coupled to Tukey's multiple test (A, C, H left panel) or Kruskal-Wallis test coupled to Dunn's multiple test (E left panel); t (p < 0.05), tt (p < 0.01), ttt (p < 0.001), tttt by Student t test or Welch's test (A, C, E left panel, I left panel).

(A) *Fgf21*

RNA levels (relative amount)

- ☐ Hept control
- ☐ Hept PA 6h
- ☐ Hept PA 6h + CM BMDM Lyzs-Cre
- ■ Hept PA 6h + CM BMDM MKK3/6$^{Lyzs-KO}$

(B) *Il12b*   *Nos2*

Fold change expression

- ☐ Lyzs-Cre ResKCs HFD
- ■ MKK3/6$^{Lyzs-KO}$ ResKCs HFD

- ☐ Lyzs-Cre MoKCs HFD
- ■ MKK3/6$^{Lyzs-KO}$ MoKCs HFD

(C)
- ☐ Lyzs-Cre BMDM
- ■ MKK3/6$^{Lyzs-KO}$ BMDM

Il12b   *Nos2*

RNA levels (relative amount)

0h   6h PA   6h PA + 8hLPS   6h PA + 16hLPS

(D)
- ☐ Lyzs-Cre BMDM
- ■ MKK3/6$^{Lyzs-KO}$ BMDM

IL-12p70 (pg/mL)

Time (hours): 0 6 12 18 24 30 36

PA   LPS

(E) *Fgf21*   *FGF21*

RNA levels (relative amount)   Fold change expression

16h   24h   p= 0.059

- ☐ Mouse hepatocyte control
- ☐ Mouse hepatocyte PA 6h
- ■ Mouse hepatocyte PA 6h+ IL-12
- ☐ THLE-2 control
- ☐ THLE-2 PA 6h
- ■ THLE-2 PA 6h + IL-12 6h

(F) Plasma

Saline   IL-12 6 hours

22 —   FGF21

FGF21

Relative amount

Saline   IL-12 6h

(G)
- ☐ Lyzs Cre HFD
- ■ MKK3/6$^{Lyzs-KO}$ HFD

Il12b

RNA levels (relative amount)

(H) AST   ALT

UI/L   UI/L

(I) Hepatocellular lesions   Level of steatosis

IL12B expression   *IL12B* expression

no lesions   Binucleation   Balloonization   Healthy   Severe

(J)

$R^2 = 0.2499$
$p = 0.0009$

IL12B expression (x10^{-4})

log AST (IU/L)

$R^2 = 0.2429$
$p = 0.0011$

IL12B expression (x10^{-4})

log ALT (UI/L)

(Figure 4G–H), suggesting a direct correlation between hepatic *Il12b* expression and liver damage in mice. Examination of human liver biopsies from patients with and without obesity revealed an association between elevated *IL12B* mRNA expression and the presence of hepatocellular lesions (binucleation and balloonization) and severe steatosis (Figure 4I). In concordance, we found a direct correlation between liver *IL12B* mRNA expression in these patients also directly correlated with the blood levels of AST and ALT (Figure 4J).

DISCUSSION

Obesity and its comorbidities (steatosis, diabetes, and metabolic diseases) are widespread human diseases that have been linked to chronic inflammation.[28]

Our results identify cross-communication between infiltrating macrophages and hepatocytes during obesity. The obesity-sensing macrophages transmit this information to hepatocytes, which produce FGF21 to activate BAT thermogenesis. The role of p38 in this physiological adaptation was unexpected, because activation of this signaling pathway in the myeloid compartment has been suggested to be detrimental and to induce steatosis.[13,14] Our data showed that complete impairment of p38 activation exacerbates the inflammatory response, leading to deleterious metabolic effects that may be due to defective macrophage adaptation.

The endocrine hormone FGF21 is mainly produced by the liver, although adipose tissue, muscle, and other organs have been shown to produce it in an autocrine manner.[29] Previous studies have described cell-autonomous regulation of FGF21 expression by stress kinases,[7,10] and neutrophil infiltration in the liver has been reported to inhibit hepatic FGF21 production.[7] Here, we found that a lack of p38 activation in liver-infiltrating macrophages signals hepatocytes to block the expression of hepatic FGF21. Macrophage–hepatocyte crosstalk resulting in the inhibition of FGF21 expression has been reported previously, with clodronate-mediated macrophage deletion shown to increase hepatic FGF21 production, promoting adipose tissue lipolysis and protecting against steatosis.[8] Our results demonstrate that this crosstalk is crucially dependent on the correct activation of p38 signaling pathway in macrophages.

Our finding shows that loss of inflammatory signals mediated by p38 activation in the myeloid compartment worsens obesity, diabetes, and steatosis. This suggests that the maintenance of whole-body homeostasis requires a precise modulation of the inflammatory response. Moreover, this discovery identifies a possible complication of drug therapies based on p38 inhibition for the treatment of chronic inflammation.

Some studies suggest that adipose tissue adaptation is mostly reliant on adipocyte FGF21.[30] However, other studies suggest that BAT activation is controlled by the endocrine action of hepatic FGF21.[23,31] In humans, a regulatory effect of hepatic FGF21 was revealed by the correlation of BAT activation with serum FGF21.[32] Our results reinforce the idea that thermogenesis is regulated principally through the action of liver FGF21.

IL-12 expression is upregulated during obesity in several tissues[33] and in the circulating blood of patients with obesity. Moreover, LPS-stimulated IL-12 production is higher in monocytes from patients with obesity than in those from lean individuals.[34] Our results suggest that IL-12 production by liver-infiltrating macrophages activates STAT and contributes to liver damage and inhibits FGF21 expression, promoting obesity. Our human cohort show a direct correlation between IL-12 expression and liver damage and suggest that the deleterious effects of IL-12 on hepatocytes play an important role promoting disease progression in patients with obesity. The direct correlation with hepatocellular damage also warrants investigation of the potential relationship between IL-12 and metabolic syndrome. Our findings raise the possibility of using commercially available anti–IL-12 antibodies for the treatment of obesity and liver disease.

AUTHOR CONTRIBUTIONS
Guadalupe Sabio conceived and supervised the overall project. Guadalupe Sabio, María Crespo, and Magdalena Leiva designed the experiments and developed the hypothesis. María Crespo and Magdalena Leiva performed the experiments, analyzed the data, and prepared Figures. Ivana Nikolic and Alfonso Mora performed experiments and assisted in analysis. Elena Rodríguez, Luis Leiva-Vega, Aránzazu Pintor-Chocano, Daniel Horrillo, Gema Medina-Gómez, Eva Novoa, and Rubén Nogueiras participated in experiments. Lourdes Hernández-Cosido, Jorge L. Torres, and Miguel Marcos provided human liver biopsies from the cohort of patients. Guadalupe Sabio, María Crespo, and Magdalena Leiva wrote the manuscript with input from all authors.

CONFLICT OF INTEREST
Nothing to report.

ETHICAL STATEMENT
All animal procedures were approved by the Animal Care and Use Committee at CNIC conformed to EU Directive 86/609/EEC and Recommendation 2007/526/EC regarding the protection of animals

ORCID

Alfonso Mora https://orcid.org/0000-0002-6397-4836
Guadalupe Sabio https://orcid.org/0000-0002-2822-0625

REFERENCES

1. Nikolic I, Leiva M, Sabio G. The role of stress kinases in metabolic disease. Nat Rev Endocrinol. 2020;16:697–716.
2. Hotamisligil GS. Inflammation, metaflammation and immunometabolic disorders. Nature. 2017;542:177–85.
3. Daemen S, Schilling JD. The interplay between tissue niche and macrophage cellular metabolism in obesity. Front Immunol. 2019;10:3133.
4. Lopez BG, Tsai MS, Baratta JL, Longmuir KJ, Robertson RT. Characterization of Kupffer cells in livers of developing mice. Comp Hepatol. 2011;10:2.
5. Alharthi J, Latchoumanin O, George J, Eslam M. Macrophages in metabolic associated fatty liver disease. World J Gastroenterol. 2020;26:1861–78.
6. Krenkel O, Tacke F. Liver macrophages in tissue homeostasis and disease. Nat Rev Immunol. 2017;17:306–21.
7. Crespo M, Gonzalez-Teran B, Nikolic I, Mora A, Folgueira C, Rodriguez E, et al. Neutrophil infiltration regulates clock-gene expression to organize daily hepatic metabolism. Elife. 2020;9:e59258.
8. Ma W, Zhao D, He F, Tang L. The role of Kupffer cells as mediators of adipose tissue lipolysis. J Immunol. 2019;203:2689–700.
9. Fisher FM, Kleiner S, Douris N, Fox EC, Mepani RJ, Verdeguer F, et al. FGF21 regulates PGC-1α and browning of white adipose tissues in adaptive thermogenesis. Genes Dev. 2012;26:271–81.
10. Vernia S, Cavanagh-Kyros J, Garcia-Haro L, Sabio G, Barrett T, Jung DY, et al. The PPARα-FGF21 hormone axis contributes to metabolic regulation by the hepatic JNK signaling pathway. Cell Metab. 2014;20:512–25.
11. Han MS, Perry RJ, Camporez JP, Scherer PE, Shulman GI, Gao G, et al. A feed-forward regulatory loop in adipose tissue promotes signaling by the hepatokine FGF21. Genes Dev. 2021;35:133–46.
12. González-Terán B, Cortés JR, Manieri E, Matesanz N, Verdugo Á, Rodríguez ME, et al. Eukaryotic elongation factor 2 controls TNF-alpha translation in LPS-induced hepatitis. J Clin Invest. 2013;123:164–78.
13. Zhang X, Fan L, Wu J, Xu H, Leung WY, Fu K, et al. Macrophage p38α promotes nutritional steatohepatitis through M1 polarization. J Hepatol. 2019;71:163–74.
14. González-Terán B, Matesanz N, Nikolic I, Verdugo MA, Sreeramkumar V, Hernández-Cosido L, et al. p38γ and p38δ reprogram liver metabolism by modulating neutrophil infiltration. EMBO J. 2016;35:536–52.
15. Risco A, del Fresno C, Mambol A, Alsina-Beauchamp D, MacKenzie KF, Yang HT, et al. p38γ and p38δ kinases regulate the toll-like receptor 4 (TLR4)-induced cytokine production by controlling ERK1/2 protein kinase pathway activation. Proc Natl Acad Sci USA. 2012;109:11200–5.
16. Kang YJ, Chen J, Otsuka M, Mols J, Ren S, Wang Y, et al. Macrophage deletion of p38alpha partially impairs lipopolysaccharide-induced cellular activation. J Immunol. 2008;180:5075–82.
17. Liu J, Zhang S, Cao H, Wang H, Sun C, Liu S, et al. Deficiency of p38α in macrophage ameliorates d-galactosamine/TNF-α-induced acute liver injury in mice. FEBS J. 2017;284:4200–15.
18. Matesanz N, Bernardo E, Acín-Pérez R, Manieri E, Pérez-Sieira S, Hernández-Cosido L, et al. MKK6 controls T3-mediated browning of white adipose tissue. Nat Commun. 2017;8:856.
19. Gonzalez-Rellan MJ, Fondevila MF, Fernandez U, Rodríguez A, Varela-Rey M, Veyrat-Durebex C, et al. O-GlcNAcylated p53 in the liver modulates hepatic glucose production. Nat Commun. 2021;12:5068.
20. González-Terán B, López JA, Rodríguez E, Leiva L, Martínez-Martínez S, Bernal JA, et al. p38γ and δ promote heart hypertrophy by targeting the mTOR-inhibitory protein DEPTOR for degradation. Nat Commun. 2016;7:10477.
21. Han MS, Jung DY, Morel C, Lakhani SA, Kim JK, Flavell RA, et al. JNK expression by macrophages promotes obesity-induced insulin resistance and inflammation. Science. 2013;339:218–22.
22. Cereijo R, Gavaldá-Navarro A, Cairó M, Quesada-López T, Villarroya J, Morón-Ros S, et al. CXCL14, a brown adipokine that mediates brown-fat-to-macrophage communication in thermogenic adaptation. Cell Metab. 2018;28:750–63.e6.
23. Stöhr O, Tao R, Miao J, Copps KD, White MF. FoxO1 suppresses Fgf21 during hepatic insulin resistance to impair peripheral glucose utilization and acute cold tolerance. Cell Rep. 2021;34:108893.
24. Remmerie A, Martens L, Thoné T, Castoldi A, Seurinck R, Pavie B, et al. Osteopontin expression identifies a subset of recruited macrophages distinct from Kupffer cells in the fatty liver. Immunity. 2020;53:641–57.e14.
25. Kong X, Horiguchi N, Mori M, Gao B. Cytokines and STATs in liver fibrosis. Front Physiol. 2012;3:69.
26. Lundåsen T, Hunt MC, Nilsson LM, Sanyal S, Angelin B, Alexson SE, et al. PPARalpha is a key regulator of hepatic FGF21. Biochem Biophys Res Commun. 2007;360:437–40.
27. Zhou YC, Waxman DJ. Cross-talk between janus kinase-signal transducer and activator of transcription (JAK-STAT) and peroxisome proliferator-activated receptor-alpha (PPARalpha) signaling pathways. Growth hormone inhibition of pparalpha transcriptional activity mediated by stat5b. J Biol Chem. 1999;274:2672–81.
28. Lee YS, Olefsky J. Chronic tissue inflammation and metabolic disease. Genes Dev. 2021;35:307–28.
29. Owen BM, Mangelsdorf DJ, Kliewer SA. Tissue-specific actions of the metabolic hormones FGF15/19 and FGF21. Trends Endocrinol Metab. 2015;26:22–9.
30. Villarroya F, Cereijo R, Villarroya J, Giralt M. Brown adipose tissue as a secretory organ. Nat Rev Endocrinol. 2017;13:26–35.
31. Sostre-Colón J, Uehara K, Garcia Whitlock AE, Gavin MJ, Ishibashi J, Potthoff MJ, et al. Hepatic AKT orchestrates adipose tissue thermogenesis via FGF21-dependent and -independent mechanisms. Cell Rep. 2021;35:109128.
32. Hanssen MJ, Broeders E, Samms RJ, Vosselman MJ, van der Lans AA, Cheng CC, et al. Serum FGF21 levels are associated with brown adipose tissue activity in humans. Sci Rep. 2015;5:10275.

33. Nam H, Ferguson BS, Stephens JM, Morrison RF. Impact of obesity on IL-12 family gene expression in insulin responsive tissues. Biochim Biophys Acta. 2013;1832:11–9.

34. Wu HP, Kuo SF, Wu SY, Chuang DY. High interleukin-12 production from stimulated peripheral blood mononuclear cells of type 2 diabetes patients. Cytokine. 2010;51:298–304.

SUPPORTING INFORMATION

Additional supporting information may be found in the online version of the article at the publisher's website.

How to cite this article: Crespo M, Nikolic I, Mora A, Rodríguez E, Leiva-Vega L, Pintor-Chocano A et al. Myeloid p38 activation maintains macrophage–liver crosstalk and BAT thermogenesis through IL-12–FGF21 axis. Hepatology. 2022;00:1–14. https://doi.org/10.1002/hep.32581